

Event patterns extracted from anisotropic spectra of charged particles produced in Pb-Pb collisions at 2.76 TeV

Ya-Hui Chen and Fu-Hu Liu*

*Institute of Theoretical Physics & State Key Laboratory of Quantum Optics and Quantum Optics Devices,
Shanxi University, Taiyuan, Shanxi 030006, China*

Abstract: Event patterns extracted from anisotropic spectra of charged particles produced in lead-lead collisions at 2.76 TeV are investigated. We use an inverse power-law resulted from the QCD calculus to describe the transverse momentum spectrum in the hard scattering process, and a revised Erlang distribution resulted from a multisource thermal model to describe the transverse momentum spectrum and anisotropic flow in the soft excitation process. The pseudorapidity distribution is described by a three-Gaussian function which is a revision of the Landau hydrodynamic model. Thus, the event patterns at the kinetic freeze-out are displayed by the scatter plots of the considered particles in the three-dimensional velocity, momentum, and rapidity spaces.

Keywords: anisotropic spectra, event patterns, three-dimensional space

PACS: 25.75.Ag, 25.75.Dw, 24.10.Pa

1 Introduction

Chemical and kinetic freeze-outs are two main stages of system evolution in high energy collisions. In the stage of chemical freeze-out, the ratios of different particle yields in the interaction system are invariant, and the collisions between (or among) these particles are inelastic. Meanwhile, the processes of particle decay and production keep in a state of dynamic equilibrium. In the stage of kinetic or thermal freeze-out, the momentum and transverse momentum distributions of different particles are invariant, and the collisions between (or among) these particles are elastic. Meanwhile, the interaction system is expected to stay in a state of thermal equilibrium.

Generally, two main stages of particle production are considered. The hard scattering is believed not to undergo the chemical freeze-out. The other stage, namely, the soft excitation process is considered undergoing the chemical and kinetic freeze-outs. The hard scattering process is actually described by the theory of strong interactions, Quantum Chromodynamics (QCD), namely by its perturbative calculations, in particular by the QCD calculus [1–3] we use here. The soft excitation process is often described by the thermal-related models [4–7] or hydrodynamic-related models [8–19].

To understand the properties of chemical and kinetic freeze-outs as well as soft process, one can use different models to describe different experimental quantities such as the particle ratio, transverse momentum

spectrum, rapidity (or pseudorapidity) spectrum, elliptic flow or higher order flow distribution, dependence of elliptic flow on transverse momentum, and others. According to these quantities, one can extract some parameters and structure the event patterns at different conditions by using the scatter plots of the considered particles. These event patterns can give us relatively whole and objective pictures of the interaction system at the freeze-outs and are helpful for us to better understand these quantities. The dependences of event patterns on the particle type, event centrality, and collision energy are particularly important and interesting.

In our previous works [20–23], the event patterns extracted from the transverse momentum and rapidity (or pseudorapidity) spectra were studied, and an isotropic assumption in the transverse plane was used. In this paper, a non-zero elliptic flow is considered in the model treatment. We use a two-component model [1–3, 24] to describe the transverse momentum spectrum and elliptic flow measurements [25–31]. A three-Gaussian function being a revision [17–19] of the Landau hydrodynamic model [32, 33], which results in a Gaussian function [8–17], is used to describe the pseudorapidity distribution. Based on the description of experimental anisotropic spectra of charged particles produced in lead-lead (Pb-Pb) collisions at the center-of-mass energy per nucleon, $\sqrt{s_{NN}}$, of 2.76 TeV [25–31], event patterns are structured in the three-dimensional velocity, momentum, and rapidity spaces.

*E-mail: fuhuliu@163.com; fuhuliu@sxu.edu.cn

2 The model and method

Before introducing the model and method, we have to structure a coordinate system and definite some variables. Let the collision point be the original O , one of the beam directions be the Oz axis, and the reaction plane be the xOz plane. We can structure a right-handed coordinate system in which the Ox axis is along the impact parameter, Oy axis is perpendicular to the xOz plane, and the transverse plane is the xOy plane. Let β_x , β_y , and β_z (p_x , p_y , and p_z) denote the velocity (momentum) components on the Ox , Oy , and Oz axes, respectively; Y_1 , Y_2 , and Y denote the rapidities defined due to energy E and p_x , E and p_y , as well as E and p_z , respectively. To obtain the event patterns in the three-dimensional velocity ($\beta_x - \beta_y - \beta_z$), momentum ($p_x - p_y - p_z$), and rapidity ($Y_1 - Y_2 - Y$) spaces at a given condition, we need at least the transverse momentum p_T and rapidity Y (or pseudorapidity η) spectra to extract the values of related parameters.

It should be noted that the elliptic flow v_2 is not zero in most cases such as in non-central collisions, which renders anisotropic flow in the xOy plane in the rest source frame. That is, the assumption of isotropic emission in the xOy plane used in our previous works [20–23] is only an approximate treatment and should be revised due to non-zero anisotropic flow. To include anisotropic flow in the event patterns, we have to use simultaneously p_T , v_2 , and Y (or η) spectra for extracting parameters and structuring event patterns. Generally, the effect of isotropic flow such as the radial flow is already included in the p_T spectrum and does not need to be considered particularly.

Generally, different models use different ideas and methods to treat the same collisions. Some of them are even inconsistent each other. The model used in the present work is a hybrid model which consists of the QCD calculus [1–3] for a wide p_T spectrum contributed by the hard scattering process, a multisource thermal model [24] for a narrow p_T spectrum contributed by the soft excitation process, and a revised Landau hydrodynamic model [17–19] for Y or η spectrum. As believed, there are generally two main processes, the hard scattering process and the soft excitation process, in particle productions in high energy collisions.

The hard scattering process happens in the early stage and between two valence quarks. Particles produced in the hard process distribute in a wide p_T range. According to the QCD calculus [1–3], the hard process contributes an inverse power-law. One has the following

function form

$$f_1(p_T) = Ap_T \left(1 + \frac{p_T}{p_0}\right)^{-n}, \quad (1)$$

where A denotes the normalization constant which depends on the free parameters p_0 and n . Because of the limitation of normalization, one has naturally $\int_0^\infty f_1(p_T) dp_T = 1$.

The soft excitation process happens in the later stage and between two (or among three or more) gluons and/or sea quarks. Particles produced in the soft process distribute in a narrow p_T range (up to 2–3 GeV/ c). According to the multisource thermal model [24], we can use the Erlang distribution

$$f_2(p_T) = \frac{p_T^{m-1}}{(m-1)! \langle p_{Ti} \rangle^m} \exp\left(-\frac{p_T}{\langle p_{Ti} \rangle}\right) \quad (2)$$

to describe the p_T spectrum contributed by the soft process, where $\langle p_{Ti} \rangle$ and m are free parameters which describe the mean contribution of each source (partons) and the number of sources (partons) respectively. Naturally, $\int_0^\infty f_2(p_T) dp_T = 1$.

Analytically, we can use a superposition of the inverse power-law and the Erlang distribution to describe the p_T spectra of final-state particles. In fact, we have the normalized distribution

$$f_0(p_T) = k_1 f_1(p_T) + (1 - k_1) f_2(p_T), \quad (3)$$

where k_1 denotes the contribution ratio of the inverse power-law, and $1 - k_1$ denotes naturally the contribution ratio of the Erlang distribution. Obviously, this superposition obeys $\int_0^\infty f_0(p_T) dp_T = 1$. To give a comparison with the non-normalized experimental data, the normalized constant (N_{p_T}) is needed.

In the Monte Carlo method, we can obtain p_T due to the above functions $f_1(p_T)$ and $f_2(p_T)$. Let R , R_0 , and r_i denote the random numbers distributed evenly in $[0, 1]$. The values of p_T in Eq. (1) or in the first component in Eq. (3) can be obtained by

$$\int_0^{p_T} f_1(p_T) dp_T < R < \int_0^{p_T + dp_T} f_1(p_T) dp_T. \quad (4)$$

The values of p_T in Eq. (2) or in the second component in Eq. (3) can be obtained by

$$p_T = -\langle p_{Ti} \rangle \sum_{i=1}^m \ln r_i = -\langle p_{Ti} \rangle \ln \prod_{i=1}^m r_i. \quad (5)$$

Then, $f_1(p_T)$, $f_2(p_T)$, and $f_0(p_T)$ can be obtained by statistics.

Under the assumption of isotropic emission, we have the momentum components in the xOy plane to be

$$p_x = p_T \cos \varphi = p_T \cos(2\pi R_0), \quad (6)$$

$$p_y = p_T \sin \varphi = p_T \sin(2\pi R_0), \quad (7)$$

where

$$\varphi = \arctan\left(\frac{p_y}{p_x}\right) = 2\pi R_0 \quad (8)$$

denotes the azimuthal angle. The isotropic emission results in the elliptic flow

$$v_2 = \langle \cos(2\varphi) \rangle = \left\langle \frac{p_x^2 - p_y^2}{p_x^2 + p_y^2} \right\rangle = 0, \quad (9)$$

where $\langle \dots \rangle$ denotes the averaging events.

However, the experimental v_2 in most cases is not equal to zero [26, 28, 34–37]. This means that, in the xOy plane, we have to consider an anisotropic emission. The anisotropic emission enlightens us to consider the interactions between (or among) the isotropic sources. These interactions result in the deformation and movement of the isotropic source. The deformation means expansion and compression, and the movement can be along the positive or negative axis direction.

Considering the deformation and movement of the source, p_x and p_y obtained above are revised to

$$P_x = a_x p_x + b_x, \quad (10)$$

$$P_y = a_y p_y + b_y, \quad (11)$$

where a_x (a_y) and b_x (b_y) denote the deformation and movement of the source in the Ox (Oy) axis direction respectively. The two equations are ascribed to the revised Erlang distribution. They reflect approximately the mean effect of interactions between (or among) the sources. The interactions are described by $a_{x,y}$ and $b_{x,y}$ which are very small and can be concretely seen in the next section. Generally, $a_{x,y} > 1$ (< 1) means an expansion (compression), $b_{x,y} > 0$ (< 0) means a movement along the positive (negative) axis direction. The introduction of $a_{x,y}$ and $b_{x,y}$ results in a revised Erlang distribution which can be obtained by the Monte Carlo method.

Because of only the relative deformation of the source being interested, we can require the minimum in a_x and a_y to be fixed to 1, and the other one to be equal to or greater than 1. Meanwhile, some sources can move along the positive axis direction, and others can move along the negative axis direction. Due to the revision on the momentum components, we have a new expression for v_2 ,

$$v_2 = \left\langle \frac{P_x^2 - P_y^2}{P_x^2 + P_y^2} \right\rangle. \quad (12)$$

The transverse momentum after the transformation is

$$p_T = \sqrt{P_x^2 + P_y^2}, \quad (13)$$

where the same symbol p_T is used as that before the transformation. Similarly, we use the symbol $p_{x,y}$ instead of $P_{x,y}$ in the following discussions even for those

after the transformation. By using v_2 and p_T , we can study the dependence of v_2 on p_T .

In the Landau hydrodynamic model and its revisions [8–19], the Y or η distribution contributed by a given source can be parameterized to a Gaussian function [8–17]. In the case of considering η distribution, we have

$$f_\eta(\eta) = \frac{1}{\sqrt{2\pi}\sigma_\eta} \exp\left[-\frac{(\eta - \eta_C)^2}{2\sigma_\eta^2}\right], \quad (14)$$

where η_C denotes the mid-pseudorapidity or peak position and σ_η denotes the distribution width. If one regards a Gaussian function for Y or η distribution as a result of the Landau hydrodynamic model, any application of two or more Gaussian functions is a revision of the model. This revision may be caused by the leading particles or resonance production.

In refs. [17, 38, 39], one uses two or three Gaussian functions to describe the Y or η distribution. In the case of using three-Gaussian function which is the case in the present work, one can write

$$\begin{aligned} f_\eta(\eta) = & \frac{k_2}{\sqrt{2\pi}\sigma_{\eta_1}} \exp\left\{-\frac{[\eta - (-\delta\eta)]^2}{2\sigma_{\eta_1}^2}\right\} \\ & + \frac{1 - 2k_2}{\sqrt{2\pi}\sigma_{\eta_2}} \exp\left[-\frac{(\eta - \eta_C)^2}{2\sigma_{\eta_2}^2}\right] \\ & + \frac{k_2}{\sqrt{2\pi}\sigma_{\eta_1}} \exp\left[-\frac{(\eta - \delta\eta)^2}{2\sigma_{\eta_1}^2}\right] \end{aligned} \quad (15)$$

for symmetric collisions, where σ_{η_1} and σ_{η_2} denote the distribution widths contributed by the backward (or forward) source and central source respectively, k_2 is the contribution ratio of the backward (or forward) source, $1 - 2k_2$ is the contribution ratio of the central source, and $-\delta\eta$ (or $\delta\eta$) is the pseudorapidity shift of the peak position for the backward (or forward) source. When comparing with experimental data, the normalization constant (N_η) is needed. It should be noted that the sources discussed in the Y or η spectra are larger than those discussed in the p_T or v_2 spectra. The two types of sources are different. It should be noted that, actually, the use of two or three Gaussian functions is somehow not a necessity, see e.g. [8–16].

In the Monte Carlo method, let R_{1-6} denote the random numbers distributed evenly in $[0, 1]$. As for the variable η in the first (backward), second (central), and third (forward) components (sources) in the three-Gaussian function, we have

$$\eta = \sigma_{\eta_1} \sqrt{-2 \ln R_1} \cos(2\pi R_2) - \delta\eta, \quad (16)$$

$$\eta = \sigma_{\eta_2} \sqrt{-2 \ln R_3} \cos(2\pi R_4) + \eta_C, \quad (17)$$

and

$$\eta = \sigma_{\eta_1} \sqrt{-2 \ln R_5} \cos(2\pi R_6) + \delta\eta, \quad (18)$$

respectively. The contribution ratios are determined by k_2 , $1 - 2k_2$, and k_2 for the first, second, and third components, respectively.

On the conversion from η to Y distributions, we perform the Monte Carlo method. According to the definition of η , i.e.

$$\eta = -\ln \tan\left(\frac{\vartheta}{2}\right), \quad (19)$$

where ϑ denotes the polar angle, we have

$$\vartheta = 2 \arctan(e^{-\eta}). \quad (20)$$

Then, the momentum component on the Oz axis is

$$p_z = p_T \cot \vartheta. \quad (21)$$

The energy is

$$E = \sqrt{p_T^2 + p_z^2 + m_0^2}, \quad (22)$$

where m_0 is the rest mass. In the case of considering charged particles, m_0 is the average weighted by rest masses and yields of different types of particles.

Further, the velocity components are

$$\beta_x = \frac{p_x}{E}, \quad (23)$$

$$\beta_y = \frac{p_y}{E}, \quad (24)$$

and

$$\beta_z = \frac{p_z}{E}. \quad (25)$$

The rapidity

$$Y = \frac{1}{2} \ln \left(\frac{E + p_z}{E - p_z} \right). \quad (26)$$

Similar to the rapidity defined by E and p_z , we define the rapidity

$$Y_1 = \frac{1}{2} \ln \left(\frac{E + p_x}{E - p_x} \right) \quad (27)$$

due to E and p_x , and the rapidity

$$Y_2 = \frac{1}{2} \ln \left(\frac{E + p_y}{E - p_y} \right) \quad (28)$$

due to E and p_y .

In the concrete calculation, we need firstly to fit the p_T distribution, dependence of v_2 on p_T , and η (or Y) distribution to get the values of free parameters and normalization constants. Then, we can use the values of free parameters obtained by the fit in the first step to get the discrete values of different kinds of kinematic variables. After repeating 1000 times calculation for each case (centrality), we can get the event patterns in three-dimensional $\beta_x - \beta_y - \beta_z$, $p_x - p_y - p_z$, and $Y_1 - Y_2 - Y$ spaces.

It should be noted that the parameterizations for the p_T and η (or Y) are independent of models, though three different models are used in the parameterizations. The parameterizations performed by us are only for the extraction of discrete values for p_T and η (or Y). Although we can use the experimental discrete values themselves, the parameterizations can extract more discrete values in wider p_T and η (or Y) ranges in the case of using the limited experimental ranges.

3 Results and discussion

Figure 1 shows the p_T dependence of the double-differential spectra, $(1/N_{EV}) \cdot 1/(2\pi p_T) \cdot d^2 N_{ch}/(d\eta dp_T)$, of charged particles produced in Pb-Pb collisions at $\sqrt{s_{NN}} = 2.76$ TeV, where N_{EV} and N_{ch} denote the numbers of events and charged particles respectively. The symbols represent the experimental data of the ALICE Collaboration [25] measured in the mid-pseudorapidity range, $|\eta| < 0.8$, with nine centrality classes, 0–5%, 5–10%, 10–20%, 20–30%, 30–40%, 40–50%, 50–60%, 60–70%, and 70–80%. The different centrality classes are scaled by different amounts marked in the panel for the purpose of clarity. The solid curves for the intermediate four cases (10–20%, 20–30%, 30–40%, and 40–50%) are our model results calculated by using the superposition of the inverse power-law and revised Erlang distribution due to Fig. 2 which will be discussed later. The dashed curves for the nine centrality classes are our model results calculated by using the superposition of the inverse power-law and (unrevised) Erlang distribution. In the calculation for charged particles, we take $m_0 = 0.174$ GeV/ c^2 which is the average rest mass obtained by us for weighting rest masses and yields of different types of particles as given in [40]. The values of free parameters (p_0 , n , k_1 , m , and $\langle p_{Ti} \rangle$) and the normalization constant (N_{pT}) for both the solid and dashed curves, χ^2 and degree of freedom ($\text{dof}|_1$) in terms of $\chi^2/\text{dof}|_1$ for the solid curves, as well as χ^2 and $\text{dof}|_2$ in terms of $\chi^2/\text{dof}|_2$ for the dashed curves are listed in Table 1. The values of $a_{x,y}$ and $b_{x,y}$ for the solid curves are listed in Table 2, which are those used in Fig. 2. For the dashed curves, we have $a_{x,y} = 1$ and $b_{x,y} = 0$. In particular, for the intermediate four cases, the solid curves are possibly not the best fitted results due to the constraint of Fig. 2 which determines $a_{x,y}$ and $b_{x,y}$, and the dashed curves are not the best fitted results due to the constraint of the solid curves in which we use simply $a_{x,y} = 1$ and $b_{x,y} = 0$ to obtain the dashed curves. The solid and dashed curves are very similar to each other in most cases. One can see that the model results describe approximately the ALICE experimental p_T spectra of

charged particles measured in different centrality classes in Pb-Pb collisions at $\sqrt{s_{NN}} = 2.76$ TeV. The effect of anisotropic flow on the p_T spectra is small and can be neglected in fact. The properties of parameters will be discussed later.

The dependences of elliptic flow $v_2\{4\}$ on p_T for charged particles produced in Pb-Pb collisions at $\sqrt{s_{NN}} = 2.76$ TeV in $|\eta| < 0.8$ for four centrality classes, 10–20%, 20–30%, 30–40%, and 40–50% are presented in Fig. 2, where $v_2\{4\}$ denotes the elliptic flow obtained by a specially appointed method [26]. Generally, different methods give different v_2 with small differences. The symbols represent the experimental data of the ALICE Collaboration [26], and the curves are our model results which are resulted from the inverse power-law which contributes zero v_2 and the revised Erlang distribution which show anisotropic flow. The parameters for the inverse power-law do not affect the results due to its zero v_2 . The parameters ($1 - k_1$, m , $\langle p_{Ti} \rangle$, $a_{x,y}$, and $b_{x,y}$), χ^2 , and dof for the revised Erlang distribution are obtained and listed in Table 1 or 2. One can see that the model results describe approximately the ALICE experimental data of the dependence of v_2 on p_T for charged particles in different centrality classes in Pb-Pb collisions at $\sqrt{s_{NN}} = 2.76$ TeV. The effect of v_2 is obvious, though its influence on the p_T spectrum is small. We shall discuss the properties of parameters later.

The p_T dependence of the double-differential spectra of positively and negatively charged pions ($\pi^+ + \pi^-$), kaons ($K^+ + K^-$), and protons plus antiprotons ($p + \bar{p}$) produced in Pb-Pb collisions at $\sqrt{s_{NN}} = 2.76$ TeV in $|\eta| < 0.8$ for eight centrality classes, 0–5%, 5–10%, 10–20%, 20–30%, 30–40%, 40–50%, 40–60%, and 60–80% are displayed in Figs. 3(a), 3(b), and 3(c), respectively. The different centrality classes are scaled by different amounts marked in the panel for the purpose of clarity. The symbols represent the experimental data of the ALICE Collaboration [27] and the solid curves for the first seven cases are our model results due to Fig. 4 which will be discussed later. For comparison, the model results corresponding to the superposition of the inverse power-law and (unrevised) Erlang distribution are displayed by the dashed curves. The values of p_0 , n , k_1 , m , $\langle p_{Ti} \rangle$, and N_{p_T} for both the solid and dashed curves, χ^2 and dof₁ for the solid curves, as well as χ^2 and dof₂ for the dashed curves are listed in Table 1. The values of $a_{x,y}$ and $b_{x,y}$ for the solid curves are listed in Table 2, which are the same as Fig. 4. For the first seven cases, the solid curves are not the best fitted results due to the constraint of Fig. 4 which determines $a_{x,y}$ and $b_{x,y}$, and the dashed curves are not the best fitted results due to

the constraint of the solid curves in which we use simply $a_{x,y} = 1$ and $b_{x,y} = 0$ to obtain the dashed curves. The sole exception is the dashed curves for the centrality 60–80% in which there is no particular constraint. One can see again that the model results describe approximately the ALICE experimental p_T spectra of identified particles measured in different centrality classes in Pb-Pb collisions at $\sqrt{s_{NN}} = 2.76$ TeV. The effect of anisotropic flow on the p_T spectrum is small and can be neglected in most cases. The parameters for the identified particle spectra are a decomposition of the parameters for the charged particle spectra. Because of the main component in charged particles being $\pi^+ + \pi^-$, the parameters for the charged particle spectra are determined by those for $\pi^+ + \pi^-$ spectra.

The dependences of elliptic flow[†] $v_2\{SP, |\Delta\eta| > 0.9\}$ on p_T for identified particles [(a) $\pi^+ + \pi^-$, (b) $K^+ + K^-$, and (c) $p + \bar{p}$] produced in Pb-Pb collisions at $\sqrt{s_{NN}} = 2.76$ TeV in $|\eta| < 0.8$ for seven centrality classes, 0–5%, 5–10%, 10–20%, 20–30%, 30–40%, 40–50%, and 50–60% are presented in Fig. 4, where $v_2\{SP, |\Delta\eta| > 0.9\}$ denotes the elliptic flow obtained by another specially appointed method [28]. The symbols represent the experimental data of the ALICE Collaboration [28], and the curves are our model results which contains the revised Erlang distribution. The parameters for the inverse power-law do not affect the results due to its zero v_2 . The parameters with χ^2 and dof for the revised Erlang distribution can be found in Tables 1 and 2 respectively. One can see again that the model results describe approximately the ALICE experimental data of the dependence of v_2 on p_T for identified particles in different centrality classes in Pb-Pb collisions at $\sqrt{s_{NN}} = 2.76$ TeV. The effect of v_2 is obvious, though its influence on the p_T spectrum is small. The parameters for $\pi^+ + \pi^-$ spectra determine those for charged particles spectra. We would like to point out that the disagreement with the data on the right side of the $v_2(p_T)$ distribution is caused by the lack for revising the inverse power-law. It is expected that an improvement can be reached if we revise the inverse power-law as what we do for the Erlang distribution. However, in this case, four more parameters will be added to the fit procedure, which complicates the study.

[†]The “SP” notation refers to the Scalar Product method [28] representing a two-particle correlation technique which uses a gap of $|\Delta\eta| > 0.9$ between the identified hadron under consideration and the reference particles.

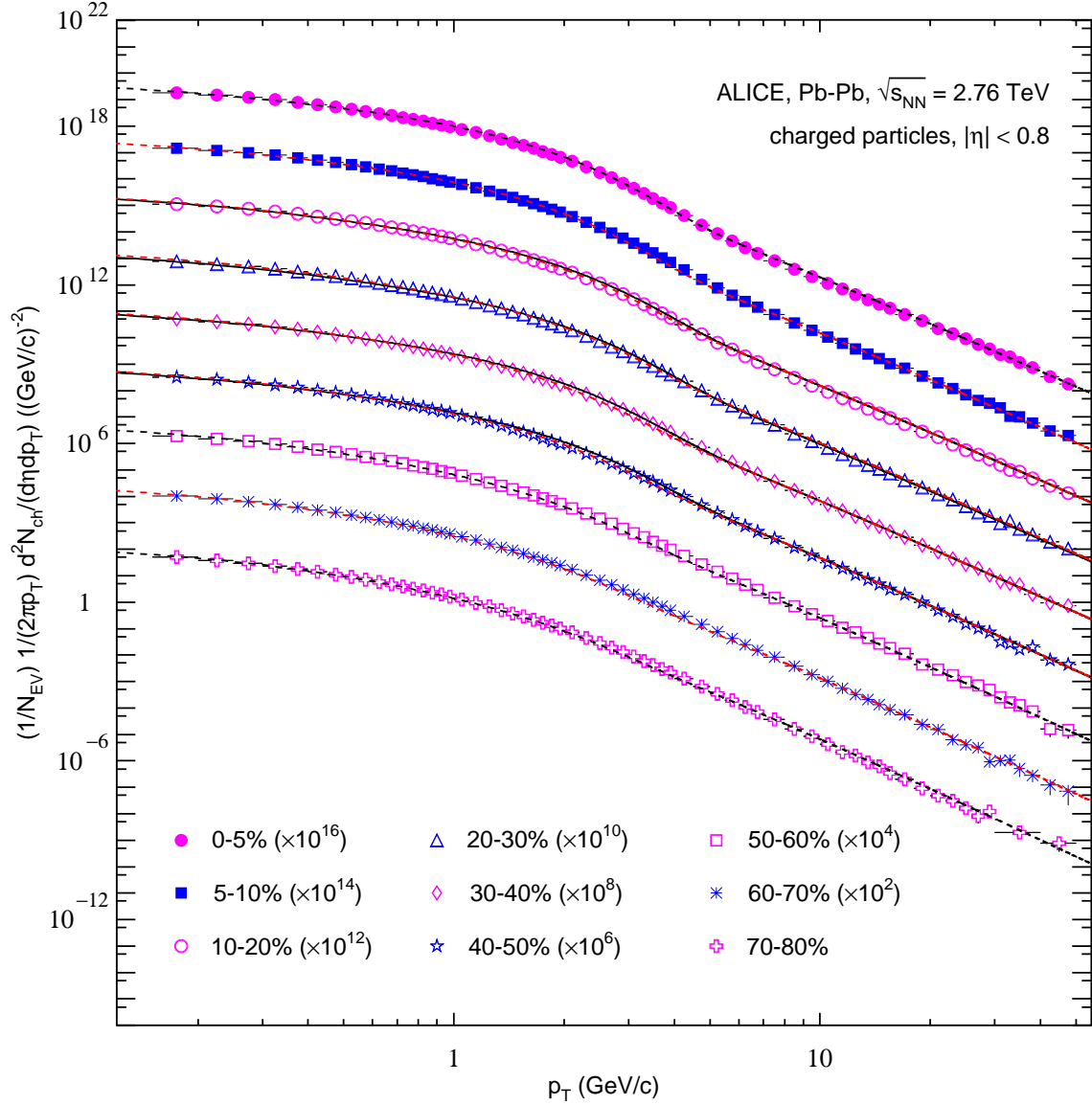


Fig. 1. Double-differential spectra of charged particles produced in Pb-Pb collisions at $\sqrt{s_{NN}} = 2.76$ TeV in the mid-pseudorapidity interval, $|\eta| < 0.8$, for nine centrality classes, 0–5%, 5–10%, 10–20%, 20–30%, 30–40%, 40–50%, 50–60%, 60–70%, and 70–80%. The different centrality classes are scaled down by different powers of ten for plot clarity. The symbols represent the experimental data of the ALICE Collaboration [25], and the solid curves for the intermediate four cases (10–20%, 20–30%, 30–40%, and 40–50%) are our model results calculated by using the superposition of the inverse power-law and revised Erlang distribution due to Fig. 2. For comparison, the model results correspond to the superposition of the inverse power-law and (unrevised) Erlang distribution are displayed by the dashed curves.

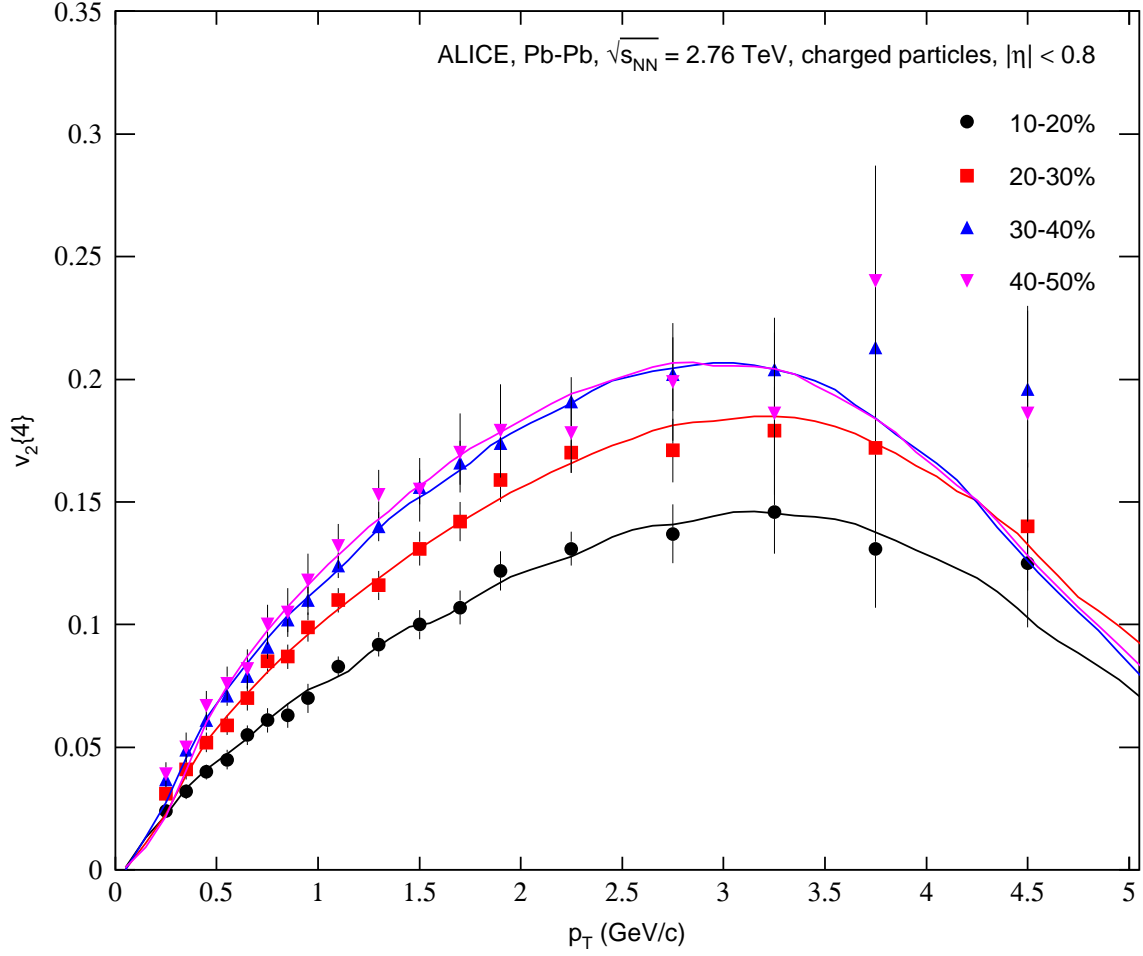


Fig. 2. Dependence of elliptic flow on transverse momentum for charged particles produced in Pb-Pb collisions at $\sqrt{s_{NN}} = 2.76$ TeV in $|\eta| < 0.8$ for four centrality classes, 10–20%, 20–30%, 30–40%, and 40–50%. The symbols represent the experimental data of the ALICE Collaboration [26], and the curves are our model results which are resulted from the inverse power-law which contributes zero elliptic flow and the revised Erlang distribution which show anisotropic flow.

Table 1. Values of free parameters (p_0 , n , k_1 , m , and $\langle p_{Ti} \rangle$) and normalization constant (N_{pT}) for both the solid and dashed curves, χ^2 and dof₁ for the solid curves, as well as χ^2 and dof₂ for the dashed curves in Figs. 1 and 3, where the values of m for Figs. 1, 3(a), 3(b), and 3(c) are invariably taken to be 2, 2, 2, and 3 respectively, which are not listed in the columns, and the values of $a_{x,y}$ and $b_{x,y}$ are the same as Fig. 2.

Figure	Centrality	p_0 (GeV/c)	n	k_1	$\langle p_{Ti} \rangle$ (GeV/c)	N_{pT}	χ^2/dof_1	χ^2/dof_2
Fig. 1	0–5%	0.64 ± 0.03	6.10 ± 0.31	0.40 ± 0.02	0.38 ± 0.01	$(2.30 \pm 0.12) \times 10^4$	–	112.114/58
	5–10%	0.64 ± 0.03	6.12 ± 0.31	0.41 ± 0.02	0.37 ± 0.01	$(2.00 \pm 0.10) \times 10^4$	–	101.732/58
	10–20%	0.66 ± 0.03	6.15 ± 0.31	0.52 ± 0.03	0.39 ± 0.01	$(1.40 \pm 0.07) \times 10^4$	94.424/58	149.176/58
	20–30%	0.67 ± 0.03	6.19 ± 0.31	0.56 ± 0.03	0.39 ± 0.01	$(9.70 \pm 0.48) \times 10^3$	81.954/58	136.474/58
	30–40%	0.70 ± 0.03	6.24 ± 0.31	0.54 ± 0.03	0.37 ± 0.01	$(6.50 \pm 0.33) \times 10^3$	72.326/58	164.256/58
	40–50%	0.73 ± 0.04	6.31 ± 0.32	0.60 ± 0.03	0.38 ± 0.01	$(3.80 \pm 0.19) \times 10^3$	103.936/58	162.214/58
	50–60%	0.77 ± 0.04	6.50 ± 0.33	0.70 ± 0.04	0.37 ± 0.01	$(2.40 \pm 0.12) \times 10^3$	–	109.214/58
	60–70%	0.77 ± 0.04	6.50 ± 0.33	0.75 ± 0.04	0.36 ± 0.01	$(1.20 \pm 0.06) \times 10^3$	–	136.358/58
	70–80%	0.81 ± 0.04	6.60 ± 0.33	0.80 ± 0.04	0.36 ± 0.01	$(5.50 \pm 0.28) \times 10^2$	–	82.012/58
Fig. 3(a)	0–5%	0.56 ± 0.03	6.10 ± 0.31	0.48 ± 0.02	0.35 ± 0.01	$(1.90 \pm 0.10) \times 10^4$	349.944/56	295.400/56
	5–10%	0.56 ± 0.03	6.12 ± 0.31	0.50 ± 0.02	0.35 ± 0.01	$(1.50 \pm 0.08) \times 10^4$	435.176/56	455.056/56
	10–20%	0.57 ± 0.03	6.15 ± 0.31	0.55 ± 0.03	0.35 ± 0.01	$(1.20 \pm 0.06) \times 10^4$	445.928/56	383.432/56
	20–30%	0.57 ± 0.03	6.19 ± 0.31	0.66 ± 0.03	0.35 ± 0.01	$(8.70 \pm 0.44) \times 10^3$	472.864/56	646.072/56
	30–40%	0.58 ± 0.03	6.22 ± 0.31	0.70 ± 0.03	0.36 ± 0.01	$(5.40 \pm 0.27) \times 10^3$	736.064/56	971.992/56
	40–50%	0.61 ± 0.03	6.30 ± 0.32	0.71 ± 0.03	0.35 ± 0.01	$(3.40 \pm 0.17) \times 10^3$	596.792/56	789.488/56
	40–60%	0.63 ± 0.03	6.40 ± 0.32	0.72 ± 0.03	0.35 ± 0.01	$(2.90 \pm 0.14) \times 10^3$	383.488/56	249.312/56
	60–80%	0.68 ± 0.03	6.50 ± 0.33	0.75 ± 0.04	0.35 ± 0.01	$(8.00 \pm 0.40) \times 10^2$	–	103.208/56
Fig. 3(b)	0–5%	1.14 ± 0.06	6.25 ± 0.31	0.10 ± 0.01	0.39 ± 0.01	3800 ± 190	128.367/51	171.768/51
	5–10%	1.14 ± 0.06	6.25 ± 0.31	0.12 ± 0.01	0.39 ± 0.01	3100 ± 155	131.682/51	202.521/51
	10–20%	1.19 ± 0.06	6.35 ± 0.32	0.15 ± 0.01	0.38 ± 0.01	2200 ± 110	114.648/51	382.449/51
	20–30%	1.19 ± 0.06	6.35 ± 0.32	0.18 ± 0.01	0.38 ± 0.01	1400 ± 85	142.188/51	489.192/51
	30–40%	1.19 ± 0.06	6.40 ± 0.32	0.20 ± 0.01	0.37 ± 0.01	950 ± 48	458.286/51	473.025/51
	40–50%	1.19 ± 0.06	6.40 ± 0.32	0.22 ± 0.01	0.36 ± 0.01	590 ± 30	351.543/51	494.853/51
	40–60%	1.19 ± 0.06	6.40 ± 0.32	0.23 ± 0.01	0.35 ± 0.01	450 ± 23	177.786/51	261.222/51
	60–80%	1.81 ± 0.09	7.30 ± 0.36	0.22 ± 0.01	0.39 ± 0.01	110 ± 6	–	84.099/51
Fig. 3(c)	0–5%	1.50 ± 0.08	6.75 ± 0.34	0.07 ± 0.01	0.41 ± 0.01	1100 ± 55	136.458/42	439.152/42
	5–10%	1.66 ± 0.08	7.05 ± 0.35	0.07 ± 0.01	0.40 ± 0.01	920 ± 46	125.244/42	594.174/42
	10–20%	1.70 ± 0.09	7.05 ± 0.34	0.07 ± 0.01	0.38 ± 0.01	720 ± 36	72.240/42	1018.668/42
	20–30%	1.70 ± 0.09	7.05 ± 0.34	0.08 ± 0.01	0.37 ± 0.01	500 ± 25	183.372/42	1132.950/42
	30–40%	1.89 ± 0.10	7.45 ± 0.38	0.11 ± 0.01	0.36 ± 0.01	310 ± 16	159.180/42	1145.382/42
	40–50%	2.02 ± 0.10	7.75 ± 0.39	0.14 ± 0.01	0.36 ± 0.01	180 ± 9	235.536/42	929.082/42
	40–60%	2.02 ± 0.10	7.75 ± 0.39	0.15 ± 0.01	0.36 ± 0.01	150 ± 7	175.686/42	327.474/42
	60–80%	2.09 ± 0.10	7.75 ± 0.39	0.15 ± 0.01	0.36 ± 0.01	45 ± 2	–	44.730/42

Figure 5 gives the η spectra of charged particles produced in Pb-Pb collisions at $\sqrt{s_{NN}} = 2.76$ TeV in ten centrality classes, 0–5%, 5–10%, 10–20%, 20–30%, 30–40%, 40–50%, 50–60%, 60–70%, 70–80%, and 80–90%. The symbols represent the experimental data of the ALICE Collaborations [29–31], where the pink, black, blue, and green symbols represent the measurements from the Silicon Pixel Detector in refs. [29] and [30], as well as from the Forward Multiplicity Detector in refs. [29] and [31], respectively. The solid curves are our results fitted by the three-Gaussian function, and the dashed curves are our results fitted by another set of parameters in the three-Gaussian function for the purpose of comparison with the solid curves. The first, second, and third Gaussian functions describe the contributions of backward, central, and forward sources (or regions or components) in the η space respectively. The values of free parameter ($\delta\eta$, $\sigma_{\eta 1}$, $\sigma_{\eta 2}$, and k_2), normalization constant (N_η), χ^2 , and dof fitted by us are listed in the upper and lower panels in Table 3 for the solid and dashed curves respectively. One can see that the model results with the two sets of parameters describe approximately the ALICE experimental η spectra of charged particles measured in different centrality classes in Pb-Pb collisions at $\sqrt{s_{NN}} = 2.76$ TeV. The η spectra obtained in different centrality classes at TeV energy confirm the three-source or other non-sole source model in high energy collisions [41–52], though the tendencies of parameters $\sigma_{\eta 1}$ and k_2 are optional, where $\sigma_{\eta 1}$ is invariant or increased and k_2 is decreased or invariant with increasing the centrality percentage. In the case of having more data in the backward (forward) η region, we can obtain the parameters as accurately as possible.

Based on the parameter values obtained from Figs. 1, 2, and 5 and listed in Tables 1–3, we can perform the Monte Carlo calculation and obtain the values of a series of kinematical quantities. Based on these kinematical quantities, we can structure some scatter plots of charged particles at the kinetic freeze-out, and these scatter plots reflect the event patterns at the last stage of the interaction process. As an example, the following discussions are only based on the upper panel of Table 3 in the case of Table 3 being used. The result based on the lower panel of Table 3 is not presented due to its triviality. In fact, what we parameterize for the p_T and η (or Y) spectra in the above is independent of models. We can even use the experimental discrete values themselves to replace these parameterizations. However, the experimental data are often measured in partly phase space. This is not enough for us to structure fully the event patterns. It is necessary to use a model for extrapolation elsewhere.

Figure 6 gives the event patterns displayed by

the scatter plots of charged particles in the three-dimensional $\beta_x - \beta_y - \beta_z$ space. The panels (a)(b), (c)(d), (e)(f), and (g)(h) correspond to the results for the centrality classes 10–20%, 20–30%, 30–40%, and 40–50%, respectively. At the same time, the left (right) panel corresponds to the results contained the revised (unrevised) Erlang distribution. The blue and red globules represent the contributions of inverse power-law and revised (unrevised) Erlang distribution respectively. The total number of charged particles for each panel is 1000. The values of root-mean-squares $\sqrt{\beta_x^2}$ for β_x , $\sqrt{\beta_y^2}$

for β_y , and $\sqrt{\beta_z^2}$ for β_z , as well as the maximum $|\beta_x|$, $|\beta_y|$, and $|\beta_z|$ (i.e. $|\beta_x|_{\max}$, $|\beta_y|_{\max}$, and $|\beta_z|_{\max}$) are listed in Table 4. One can see that, for the four centrality classes, the event patterns displayed by the scatter plots of charged particles in the three-dimensional $\beta_x - \beta_y - \beta_z$ space are rough sphericity (or fat ellipsoid along the Oz axis) with high density close to $\beta_z = 1$. In particular, $\sqrt{\beta_y^2} \leq \sqrt{\beta_x^2} < \sqrt{\beta_z^2}$ and $|\beta_y|_{\max} \approx |\beta_x|_{\max} \approx |\beta_z|_{\max}$.

Figure 7 is the same as Fig. 6, but it shows the event patterns in the three-dimensional $p_x - p_y - p_z$ space. The values of root-mean-squares $\sqrt{p_x^2}$ for p_x , $\sqrt{p_y^2}$ for p_y , and $\sqrt{p_z^2}$ for p_z , as well as the maximum $|p_x|$, $|p_y|$, and $|p_z|$ (i.e. $|p_x|_{\max}$, $|p_y|_{\max}$, and $|p_z|_{\max}$) are listed in Table 5. One can see that, for the four centrality classes, if the relative large size in the p_z direction is considered, the event patterns in the three-dimensional $p_x - p_y - p_z$ space can be regarded as rough cylinders with some removed particles from the profile. In particular, $\sqrt{p_y^2} \leq \sqrt{p_x^2} \ll \sqrt{p_z^2}$ and $|p_y|_{\max} \approx |p_x|_{\max} \ll |p_z|_{\max}$.

Figure 8 is also the same as Fig. 6, but it shows the event patterns in the three-dimensional $Y_1 - Y_2 - Y$ space. The values of root-mean-squares $\sqrt{Y_1^2}$ for Y_1 , $\sqrt{Y_2^2}$ for Y_2 , and $\sqrt{Y^2}$ for Y , as well as the maximum $|Y_1|$, $|Y_2|$, and $|Y|$ (i.e. $|Y_1|_{\max}$, $|Y_2|_{\max}$, and $|Y|_{\max}$) are listed in Table 6. One can see that, for the four centrality classes, the event patterns in the three-dimensional $Y_1 - Y_2 - Y$ space are rough cylinder with a high peak at the top and a long tail at the bottom. In particular, $\sqrt{Y_2^2} \leq \sqrt{Y_1^2} < \sqrt{Y^2}$ and $|Y_2|_{\max} \approx |Y_1|_{\max} < |Y|_{\max}$.

Table 2. Values of free parameters (a_x , b_x , a_y , and b_y), χ^2 , and dof corresponding to the curves in Figs. 2 and 4. These parameters consists of the revised Erlang distribution. The parameters b_x and b_y can take simultaneously positive and negative values. Both the probabilities for positive and negative $b_{x,y}$ are 50%. The solid curves contained the revised Erlang distribution in Fig. 1 also use the same parameters as Fig. 2.

Figure	Centrality	a_x	$\pm b_x$	a_y	$\pm b_y$	χ^2/dof
Fig. 2	10–20%	1.09 ± 0.01	0.23 ± 0.01	1.00 ± 0.01	0.00 ± 0.01	5.304/8
	20–30%	1.11 ± 0.01	0.29 ± 0.01	1.00 ± 0.01	0.00 ± 0.01	13.632/8
	30–40%	1.14 ± 0.01	0.30 ± 0.01	1.00 ± 0.01	0.00 ± 0.01	20.488/8
	40–50%	1.14 ± 0.01	0.35 ± 0.01	1.00 ± 0.01	0.00 ± 0.01	21.136/8
Fig. 4(a)	0–5%	1.04 ± 0.01	0.10 ± 0.01	1.00 ± 0.01	0.00 ± 0.01	150.162/29
	5–10%	1.06 ± 0.01	0.20 ± 0.01	1.00 ± 0.01	0.00 ± 0.01	162.980/29
	10–20%	1.10 ± 0.01	0.24 ± 0.01	1.00 ± 0.01	0.00 ± 0.01	248.675/29
	20–30%	1.12 ± 0.01	0.35 ± 0.01	1.00 ± 0.01	0.00 ± 0.01	287.419/29
	30–40%	1.12 ± 0.01	0.42 ± 0.01	1.00 ± 0.01	0.00 ± 0.01	449.500/29
	40–50%	1.13 ± 0.01	0.43 ± 0.01	1.00 ± 0.01	0.00 ± 0.01	472.178/29
	50–60%	1.13 ± 0.01	0.43 ± 0.01	1.00 ± 0.01	0.00 ± 0.01	462.115/29
Fig. 4(b)	0–5%	1.05 ± 0.01	0.03 ± 0.01	1.00 ± 0.01	0.01 ± 0.01	87.494/22
	5–10%	1.09 ± 0.01	0.04 ± 0.01	1.00 ± 0.01	0.01 ± 0.01	130.438/22
	10–20%	1.14 ± 0.01	0.06 ± 0.01	1.00 ± 0.01	0.01 ± 0.01	184.734/22
	20–30%	1.19 ± 0.01	0.11 ± 0.01	1.00 ± 0.01	0.09 ± 0.01	232.232/22
	30–40%	1.18 ± 0.01	0.45 ± 0.01	1.00 ± 0.01	0.33 ± 0.01	197.318/22
	40–50%	1.18 ± 0.01	0.44 ± 0.01	1.00 ± 0.01	0.31 ± 0.01	177.870/22
	50–60%	1.16 ± 0.01	0.47 ± 0.01	1.00 ± 0.01	0.33 ± 0.01	130.460/22
Fig. 4(c)	0–5%	1.05 ± 0.01	0.33 ± 0.01	1.00 ± 0.01	0.30 ± 0.01	73.467/27
	5–10%	1.08 ± 0.01	0.36 ± 0.01	1.00 ± 0.01	0.30 ± 0.01	101.142/27
	10–20%	1.10 ± 0.01	0.49 ± 0.01	1.00 ± 0.01	0.36 ± 0.01	131.679/27
	20–30%	1.11 ± 0.01	0.57 ± 0.02	1.00 ± 0.01	0.36 ± 0.01	151.065/27
	30–40%	1.13 ± 0.01	0.59 ± 0.02	1.00 ± 0.01	0.35 ± 0.01	159.813/27
	40–50%	1.13 ± 0.01	0.60 ± 0.02	1.00 ± 0.01	0.30 ± 0.01	144.234/27
	50–60%	1.11 ± 0.01	0.60 ± 0.02	1.00 ± 0.01	0.26 ± 0.01	186.219/27

Table 3. Upper panel: Values of free parameter ($\delta\eta$, $\sigma_{\eta 1}$, $\sigma_{\eta 2}$, and k_2), normalization constant (N_η), χ^2 , and dof corresponding to the solid curves in Fig. 5, where $\eta_C = 0$ is not listed in the column. Lower panel: Same as the upper panel, but showing the values corresponding to the dashed curves in Fig. 5.

Type	Centrality	$\delta\eta$	$\sigma_{\eta 1}$	$\sigma_{\eta 2}$	k_2	N_η	χ^2/dof
Solid Curves	0–5%	2.18 ± 0.11	1.80 ± 0.09	8.00 ± 1.00	0.21 ± 0.01	$(1.60 \pm 0.08) \times 10^5$	6.462/37
	5–10%	2.18 ± 0.11	1.80 ± 0.09	8.00 ± 1.00	0.21 ± 0.01	$(1.31 \pm 0.07) \times 10^5$	5.360/37
	10–20%	2.20 ± 0.11	1.82 ± 0.09	8.60 ± 1.00	0.19 ± 0.01	$(1.00 \pm 0.05) \times 10^5$	5.278/37
	20–30%	2.20 ± 0.11	1.80 ± 0.09	8.60 ± 1.00	0.19 ± 0.01	$(6.80 \pm 0.34) \times 10^4$	4.007/37
	30–40%	2.22 ± 0.11	1.80 ± 0.09	9.00 ± 1.00	0.17 ± 0.01	$(4.40 \pm 0.22) \times 10^4$	3.535/29
	40–50%	2.22 ± 0.11	1.80 ± 0.09	9.10 ± 1.00	0.17 ± 0.01	$(2.70 \pm 0.14) \times 10^4$	5.485/29
	50–60%	2.32 ± 0.12	1.82 ± 0.09	10.00 ± 1.00	0.17 ± 0.01	$(1.56 \pm 0.08) \times 10^4$	3.786/29
	60–70%	2.40 ± 0.12	1.82 ± 0.09	10.00 ± 1.00	0.16 ± 0.01	$(8.20 \pm 0.41) \times 10^3$	6.990/29
	70–80%	2.43 ± 0.12	1.82 ± 0.09	10.00 ± 1.00	0.15 ± 0.01	$(3.80 \pm 0.19) \times 10^3$	9.934/29
80–90%	2.48 ± 0.13	1.82 ± 0.09	10.00 ± 1.00	0.14 ± 0.01	$(1.50 \pm 0.07) \times 10^3$	9.909/28	
Dashed Curves	0–5%	2.17 ± 0.11	1.84 ± 0.09	8.00 ± 1.00	0.21 ± 0.01	$(1.60 \pm 0.08) \times 10^5$	5.388/37
	5–10%	2.20 ± 0.11	1.86 ± 0.09	8.00 ± 1.00	0.21 ± 0.01	$(1.31 \pm 0.07) \times 10^5$	3.763/37
	10–20%	2.24 ± 0.11	1.86 ± 0.09	8.00 ± 1.00	0.21 ± 0.01	$(1.00 \pm 0.05) \times 10^5$	6.092/37
	20–30%	2.27 ± 0.11	1.86 ± 0.09	8.00 ± 1.00	0.21 ± 0.01	$(6.80 \pm 0.34) \times 10^4$	3.306/37
	30–40%	2.30 ± 0.11	1.86 ± 0.09	9.00 ± 1.00	0.21 ± 0.01	$(4.40 \pm 0.22) \times 10^4$	4.020/29
	40–50%	2.33 ± 0.11	1.88 ± 0.09	9.00 ± 1.00	0.21 ± 0.01	$(2.70 \pm 0.14) \times 10^4$	3.759/29
	50–60%	2.38 ± 0.12	1.88 ± 0.09	10.00 ± 1.00	0.21 ± 0.01	$(1.56 \pm 0.08) \times 10^4$	3.880/29
	60–70%	2.44 ± 0.12	1.90 ± 0.09	10.00 ± 1.00	0.21 ± 0.01	$(8.20 \pm 0.41) \times 10^3$	7.169/29
	70–80%	2.47 ± 0.12	1.91 ± 0.09	10.00 ± 1.00	0.21 ± 0.01	$(3.80 \pm 0.19) \times 10^3$	7.760/29
80–90%	2.51 ± 0.13	1.96 ± 0.09	10.00 ± 1.00	0.21 ± 0.01	$(1.50 \pm 0.07) \times 10^3$	15.671/28	

Table 4. Values of the root-mean-squares $\sqrt{\beta_x^2}$ for β_x , $\sqrt{\beta_y^2}$ for β_y , and $\sqrt{\beta_z^2}$ for β_z , as well as the maximum $|\beta_x|$, $|\beta_y|$, and $|\beta_z|$ (i.e. $|\beta_x|_{\max}$, $|\beta_y|_{\max}$, and $|\beta_z|_{\max}$) corresponding to the scatter plots in Figs. 6(a)(b)–6(g)(h) which show 2.76 TeV Pb-Pb collisions with centrality classes 10–20%, 20–30%, 30–40%, and 40–50%, respectively. The upper panel in the table is the results presented in the left panel in the figure and contained the revised Erlang distribution, and the lower panel in the table is the results presented in the right panel in the figure and contained the (unrevised) Erlang distribution. Both the root-mean-squares and the maximum velocity components are in the units of c .

Type	Centrality	$\sqrt{\beta_x^2}$	$\sqrt{\beta_y^2}$	$\sqrt{\beta_z^2}$	$ \beta_x _{\max}$	$ \beta_y _{\max}$	$ \beta_z _{\max}$
Revised Erlang	10–20%	0.264 ± 0.009	0.264 ± 0.010	0.897 ± 0.005	0.931	0.976	1.000
	20–30%	0.278 ± 0.010	0.263 ± 0.009	0.888 ± 0.005	0.983	0.979	1.000
	30–40%	0.278 ± 0.010	0.240 ± 0.009	0.901 ± 0.005	0.970	0.949	1.000
	40–50%	0.279 ± 0.009	0.264 ± 0.009	0.890 ± 0.006	0.963	0.947	1.000
Unrevised Erlang	10–20%	0.254 ± 0.009	0.268 ± 0.010	0.895 ± 0.005	0.897	0.987	1.000
	20–30%	0.267 ± 0.009	0.268 ± 0.009	0.886 ± 0.006	0.964	0.994	1.000
	30–40%	0.269 ± 0.010	0.244 ± 0.009	0.901 ± 0.005	0.972	0.954	1.000
	40–50%	0.265 ± 0.009	0.271 ± 0.009	0.888 ± 0.006	0.963	0.984	1.000

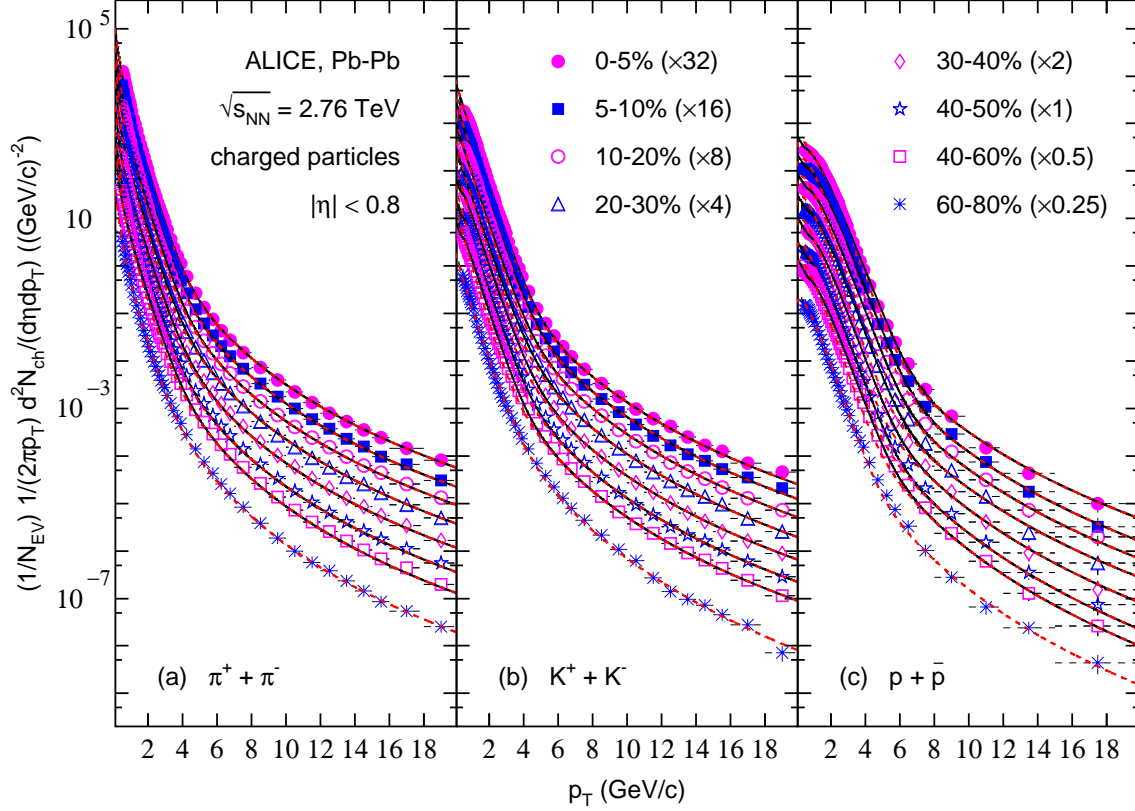


Fig. 3. Double-differential spectra of charged (a) pions ($\pi^+ + \pi^-$), (b) kaons ($K^+ + K^-$), and (c) (anti)protons ($p + \bar{p}$) produced in Pb-Pb collisions at $\sqrt{s_{NN}} = 2.76$ TeV in $|\eta| < 0.8$ for eight centrality classes, 0–5%, 5–10%, 10–20%, 20–30%, 30–40%, 40–50%, 40–60%, and 60–80%. The different centrality classes are scaled down by different factors listed in the panel for plot clarity. The symbols represent the experimental data of the ALICE Collaboration [27] and the solid curves for the first seven cases are our model results due to Fig. 4. For comparison, the model results correspond to the superposition of the inverse power-law and (unrevised) Erlang distribution are displayed by the dashed curves.

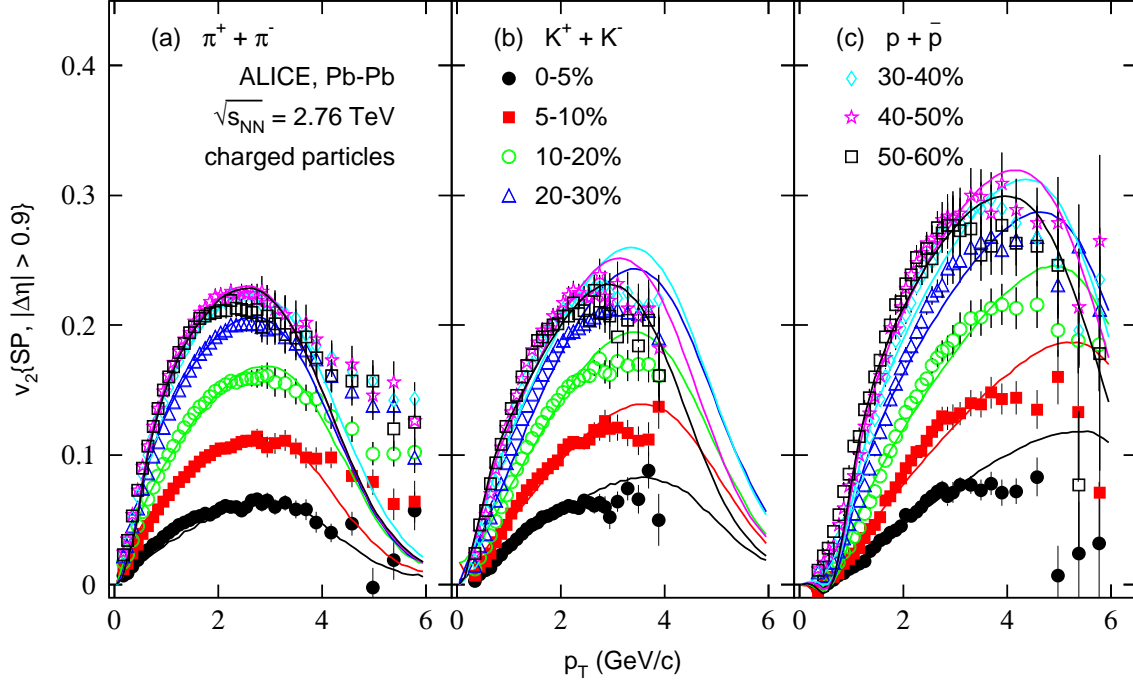


Fig. 4. Dependence of elliptic flow on transverse momentum for (a) $\pi^+ + \pi^-$, (b) $K^+ + K^-$, and (c) $p + \bar{p}$ produced in Pb-Pb collisions at $\sqrt{s_{NN}} = 2.76$ TeV in $|\eta| < 0.8$ for seven centrality classes, 0–5%, 5–10%, 10–20%, 20–30%, 30–40%, 40–50%, and 50–60%. The symbols represent the experimental data of the ALICE Collaboration [28] and the curves are our model results contained the revised Erlang distribution.

From Figs. 1–4 and Tables 1 and 2, one can see that the effect of anisotropic emission in the transverse plane on the p_T spectra is not obvious, though v_2 is large in the considered four centrality classes. With increasing the centrality percentage from 0% to 60% or 80%, the parameters p_0 , n , and k_1 increase, which reflects that the strength and fraction of the hard process increase from the central to peripheral collisions due to the decreasing participant region in the interaction system and secondary cascade collisions in the soft process. At the same time, the parameter $\langle p_{Ti} \rangle$ decreases or does not change approximately from the central to peripheral collisions, which reflects the less or nearly invariant energy deposition with increasing the centrality percentage due to the limiting secondary cascade collisions. It is natural or may be coincidental that the value of m is equal to the number of quarks in identified particles. That is why $m = 2$, 2, and 3 correspond to the productions of $\pi^+ + \pi^-$, $K^+ + K^-$, and $p + \bar{p}$, respectively.

From central to peripheral collisions, the parameters a_x and $|b_x|$ increase, the parameter a_y is fixed to 1 due to our requirement, and the parameter $|b_y|$ increases or does not change approximately. These tendencies reflect that the source has a larger expansion along the Ox axis in peripheral collisions than that in central collisions. The source has also a larger movement along the Ox

axis or in the planes of the first and third quadrants in peripheral collisions than that in central collisions. The larger expansion and movement of the source in peripheral collisions are resulted from the larger asymmetry in geometry and mechanics. In addition, less participant region and secondary cascade collisions in peripheral collisions can reduce the interactions between or among different sources, which can also reduce the probability for isotropy. As a result, peripheral collisions present a more obvious anisotropic spectrum.

Although we have used the Erlang distribution to describe the p_T spectrum produced in the soft process, many other functions can be used in the fit process, too. These functions include, but are not limited to, the two-component standard (Boltzmann, Fermi-Dirac, and Bose-Einstein) distribution [53], the Tsallis distribution with different forms [53, 54], the distribution of blast-wave model with different statistics [55, 56], etc. To revise these functions for describing $v_2(p_T)$ distribution, we can perform the same or similar treatment as what we do for the Erlang distribution. In particular, the Tsallis distribution can fit the sum of two- and even three-component standard distribution [57, 58], which reveals the advantage of the Tsallis distribution. However, the physics essence of the Tsallis distribution is needed to undergo more studies. The relation between

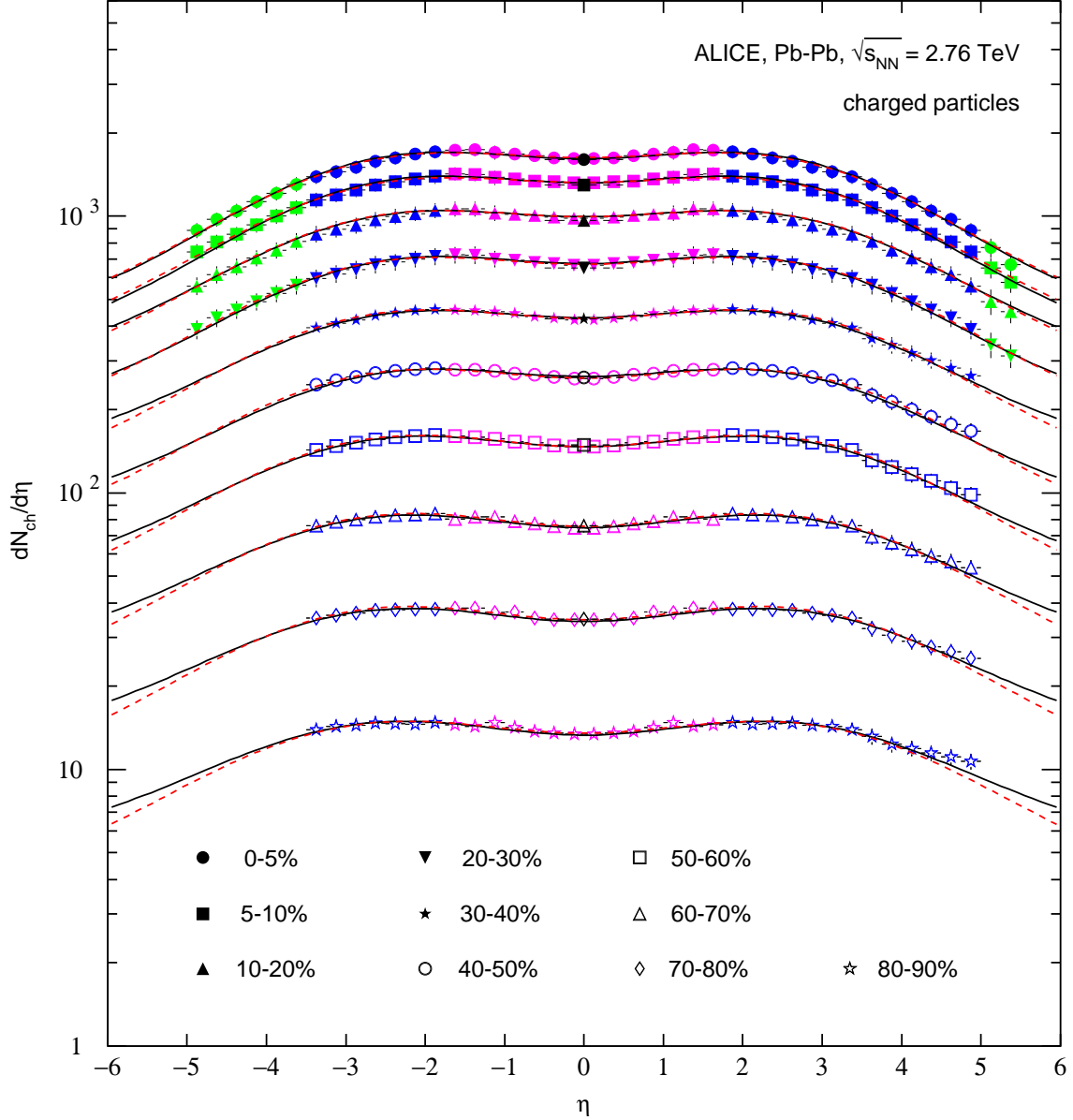


Fig. 5. Pseudorapidity spectra of charged particles produced in Pb-Pb collisions at $\sqrt{s_{NN}} = 2.76$ TeV in ten centrality classes, 0–5%, 5–10%, 10–20%, 20–30%, 30–40%, 40–50%, 50–60%, 60–70%, 70–80%, and 80–90%. The symbols represent the experimental data of the ALICE Collaborations [29–31], where the pink, black, blue, and green symbols represent the measurements from the Silicon Pixel Detector in refs. [29] and [30], as well as from the Forward Multiplicity Detector in refs. [29] and [31], respectively. The solid and dashed curves are our results fitted by the three-Gaussian function with two different sets of parameters.

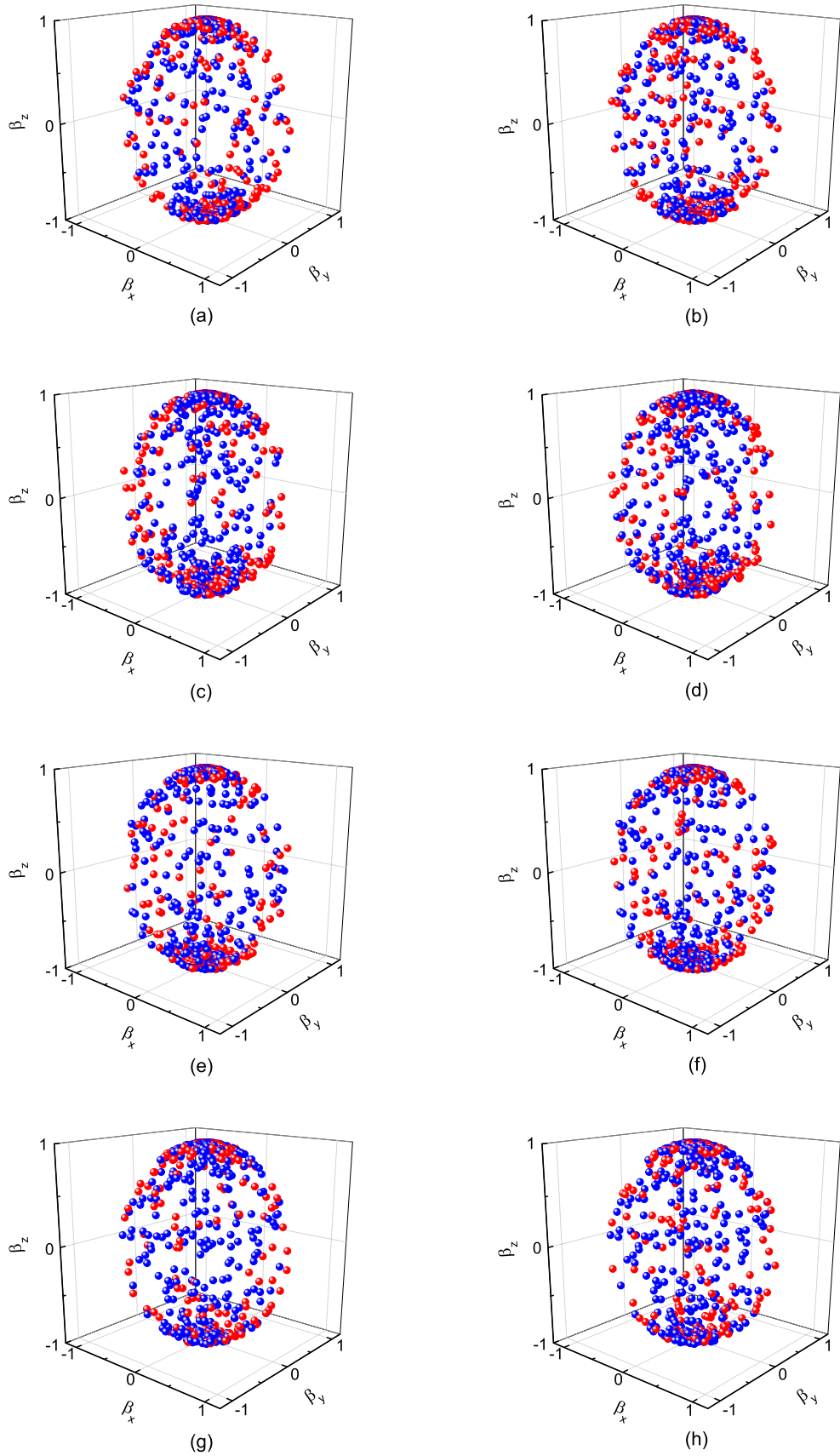


Fig. 6. Event patterns displayed by the scatter plots of charged particles in three-dimensional velocity ($\beta_x - \beta_y - \beta_z$) space in Pb-Pb collisions at $\sqrt{s_{NN}} = 2.76$ TeV in four centrality classes (a)(b) 10–20%, (c)(d) 20–30%, (e)(f) 30–40%, and (g)(h) 40–50%. The number of charged particles for each panel is 1000. The blue and red globules in the left panel represent the contributions of the inverse power-law and revised Erlang distribution for p_T respectively, and those in the right panel correspond to the contributions of the inverse power-law and (unrevised) Erlang distribution. The blue globules presented in the left and right panels are totally the same, and the red globules presented in both the panels are similar to each other.

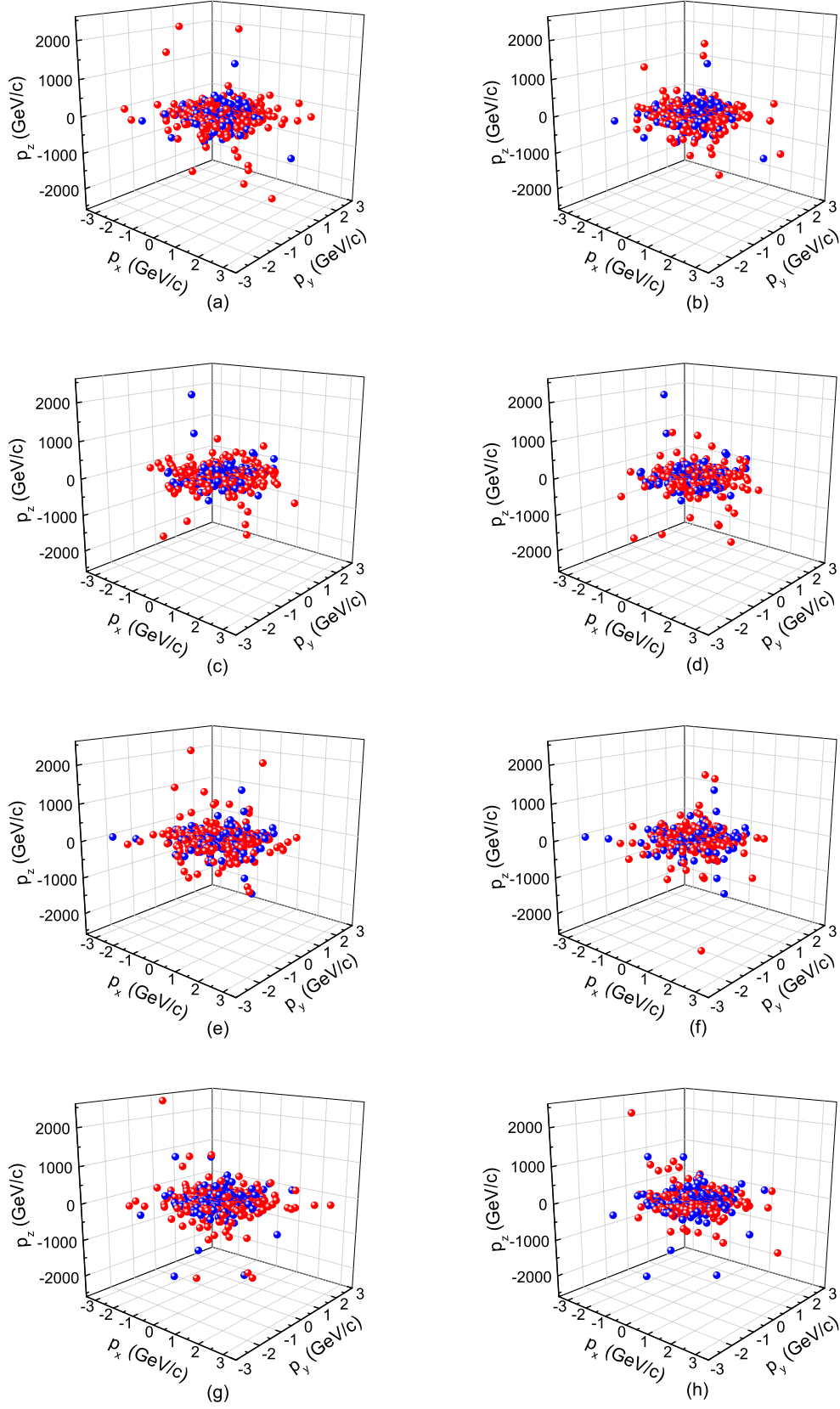


Fig. 7. Same as Fig. 6, but showing the results in three-dimensional momentum ($p_x - p_y - p_z$) space.

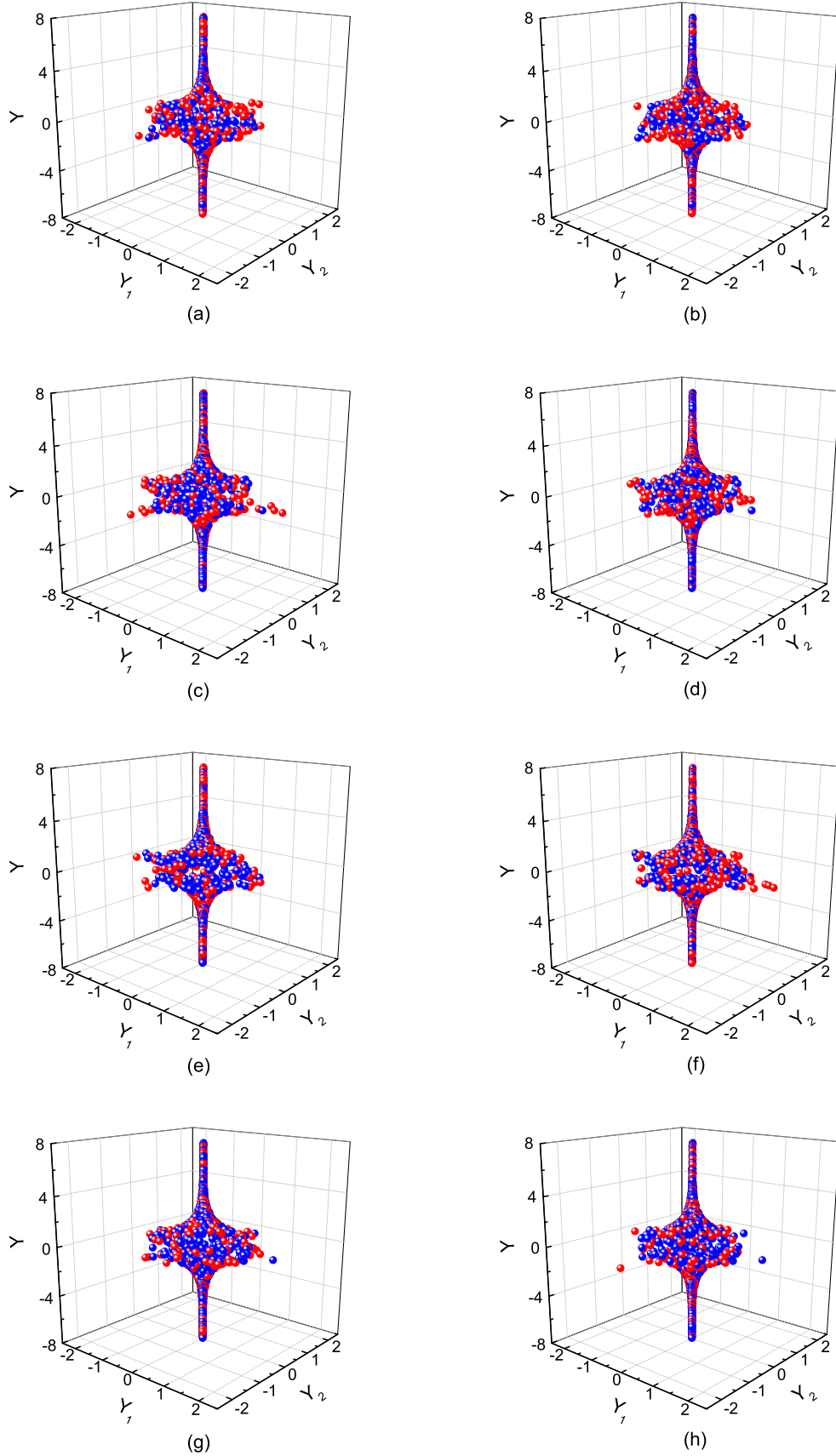


Fig. 8. Same as Fig. 6, but showing the results in three-dimensional rapidity ($Y_1 - Y_2 - Y$) space.

Table 5. Same as Table 4, but showing the values of the root-mean-squares $\sqrt{p_x^2}$ for p_x , $\sqrt{p_y^2}$ for p_y , and $\sqrt{p_z^2}$ for p_z , as well as the maximum $|p_x|$, $|p_y|$, and $|p_z|$ (i.e. $|p_x|_{\max}$, $|p_y|_{\max}$, and $|p_z|_{\max}$) corresponding to the scatter plots in Fig. 7. All the root-mean-squares and the maximum momentum components are in the units of GeV/c.

Type	Centrality	$\sqrt{p_x^2}$	$\sqrt{p_y^2}$	$\sqrt{p_z^2}$	$ p_x _{\max}$	$ p_y _{\max}$	$ p_z _{\max}$
Revised Erlang	10–20%	0.626 ± 0.028	0.557 ± 0.022	210.9 ± 25.2	4.876	2.807	2444.7
	20–30%	0.613 ± 0.024	0.537 ± 0.032	163.2 ± 19.6	3.390	5.340	1967.4
	30–40%	0.620 ± 0.022	0.505 ± 0.019	197.6 ± 21.1	3.130	2.292	2237.6
	40–50%	0.637 ± 0.024	0.589 ± 0.025	222.2 ± 23.9	3.061	3.554	2583.9
Unrevised Erlang	10–20%	0.567 ± 0.025	0.557 ± 0.022	197.3 ± 22.5	4.263	2.807	2219.9
	20–30%	0.540 ± 0.022	0.537 ± 0.032	152.1 ± 20.2	3.390	5.340	1967.4
	30–40%	0.546 ± 0.021	0.505 ± 0.019	168.4 ± 17.2	3.130	2.292	1736.7
	40–50%	0.547 ± 0.020	0.589 ± 0.025	204.2 ± 20.5	2.460	3.554	1965.5

Table 6. Same as Table 4, but showing the values of the root-mean-squares $\sqrt{Y_1^2}$ for Y_1 , $\sqrt{Y_2^2}$ for Y_2 , and $\sqrt{Y^2}$ for Y , as well as the maximum $|Y_1|$, $|Y_2|$, and $|Y|$ (i.e. $|Y_1|_{\max}$, $|Y_2|_{\max}$, and $|Y|_{\max}$) corresponding to the scatter plots in Fig. 8.

Type	Centrality	$\sqrt{Y_1^2}$	$\sqrt{Y_2^2}$	$\sqrt{Y^2}$	$ Y_1 _{\max}$	$ Y_2 _{\max}$	$ Y _{\max}$
Revised Erlang	10–20%	0.327 ± 0.014	0.349 ± 0.019	3.575 ± 0.067	1.665	2.203	8.060
	20–30%	0.368 ± 0.019	0.341 ± 0.018	3.522 ± 0.065	2.373	2.284	7.918
	30–40%	0.368 ± 0.018	0.295 ± 0.015	3.656 ± 0.066	2.088	1.817	8.015
	40–50%	0.357 ± 0.016	0.339 ± 0.016	3.582 ± 0.068	1.985	1.803	7.996
Unrevised Erlang	10–20%	0.306 ± 0.013	0.357 ± 0.020	3.569 ± 0.067	1.458	2.523	8.045
	20–30%	0.338 ± 0.016	0.353 ± 0.021	3.509 ± 0.065	1.997	2.928	7.866
	30–40%	0.351 ± 0.018	0.301 ± 0.015	3.637 ± 0.066	2.129	1.876	8.033
	40–50%	0.331 ± 0.015	0.349 ± 0.017	3.573 ± 0.068	1.985	2.425	7.996

the temperatures obtained from the standard distribution and the Tsallis distribution is also of interest [57, 58].

From Fig. 5 and Table 3 one can see that, the central region or source contributes a wide and major η spectrum, which is resulted from the Landau hydrodynamic model [8–19]. The backward (forward) region or source contributes a narrow and minor η spectrum, which is a revision for the Landau hydrodynamic model. The distribution widths contributed by the central and backward (forward) sources in central collisions are less than or equal to those in peripheral collisions due to the stronger stopping power of nucleus in central collisions or the effect of leading nucleons. The η shift of the backward (forward) source in central collisions is less than that in peripheral collisions due to the stronger stopping power. The stronger stopping power corresponds to the weaker penetrating power and narrower η spectrum. Comparing with peripheral collisions, more resonances are produced in leading nucleons in the backward (forward) source in central collisions due to more multiple scatterings undergone by the leading nucleons, though more particles can be produced in central collisions due to more energy depositions. As a competitive result, it is possible that the contribution ratio of the backward (forward) source in central collisions is greater than or equal to that in peripheral collisions.

It should be noted that although we have used a three-Gaussian function to describe the η spectrum in Fig. 5, it is of course not a sole and necessary choice. In

fact, different pictures and functions are used in different models to obtain the same or similar results. Even different functions are used in the same or similar hydrodynamic model [13–19]. In particular, in refs. [13, 16] where no leading nucleons or stopping effects are included while the distributions are well described. In refs. [14–16], the participant dissipating energy picture is used and the distributions are well described, too. However, in refs. [17–19], two sources of leading particles are included in the distributions. One of them contributes a Gaussian function in the backward region and another one contributes a Gaussian function in the forward region.

Moreover, although we study Pb-Pb collisions in the present work, the same or similar method can be used in studies of proton-proton and proton-nucleus collisions (with high multiplicity) due to similarity of experimental spectra [21, 52, 59]. The similar experimental spectrum for different types of collisions at high energy reveals some universality in hadroproduction process, as it is argued in refs. [14–16, 60, 61]. The universality in hadroproduction process appears in different quantities measured [62] in different types of collisions and/or at different energies. These quantities include, but are not limited to, mean multiplicity, rapidity or pseudorapidity density, multiplicity or transverse momentum distributions.

Combining Figs. 6–8 and Tables 4–6, one can see that the effect of anisotropic emission in the transverse plane on the event patterns is not obvious, though v_2

is large in the considered four centrality classes. In the considered four centrality classes, the root-mean-squares and maximums for velocity, momentum, and rapidity components do not depend on the centrality obviously. Because of the anisotropic emission in the transverse plane, we obtain a less root-mean-square in the y component than that in the x component. In the case of considering isotropic emission in the transverse plane, we can obtain equivalent root-mean-squares in both the y and x components.

It is expected that the event patterns displayed by the scatter plots of different particles produced in different centralities at different energies have some similarities or differences. In particular, the event patterns displayed by the scatter plots of charged particles in the three-dimensional velocity space are rough sphericity (or fat ellipsoid along Oz axis) with high density close to $\beta_z = 1$ [22]. This rough sphericity does not depend obviously on the centrality at dozens of GeV and above. The event patterns displayed by the scatter plots of Z bosons or top and anti-top systems are rough cylinder [21, 23]. This rough cylinder does not depend obviously on the centrality in the energy range mentioned above.

4 Conclusions

We summarize here our main observations and conclusions.

a) We have used the hybrid model to fit the p_T spectra, dependence of v_2 on p_T , and η spectra of charged particles produced in Pb-Pb collisions at $\sqrt{s_{NN}} = 2.76$ TeV. At the same time, the p_T spectra and dependence of v_2 on p_T for identified particles are fitted by the model. The model results are approximately in agreement with the experimental data of the ALICE Collaboration. All parameter values and event patterns extracted from the fits reflect the properties of interaction system at the stage of kinetic freeze-out, but not those at the stage of chemical freeze-out, due to these values and patterns being extracted from the p_T and η spectra as well as dependence of v_2 on p_T .

b) From central to peripheral collisions, the strength and fraction of the hard process increase and the energy deposition decreases or is nearly invariant. The emission source in peripheral collisions has a larger expansion along the Ox axis, and has also a larger movement along the Ox axis or in the planes of the first and third quadrants. Finally, peripheral collisions present a more obvious anisotropic spectrum. Although v_2 is large in some cases, the effect of anisotropic emission in the transverse plane on the p_T spectra is not obvious.

c) In the fit to η spectra by the three-Gaussian function, the central source contributes a wide and major η spectrum, and the backward (forward) source contributes a narrow and minor η spectrum. In central collisions, the distributions contributed by the central and backward (forward) sources have a less or invariant width and the η shift of the backward (forward) source is less. Meanwhile, more resonances are produced in leading nucleons in the backward (forward) source, though more particles can be produced. As a competitive result, the contribution ratio of the backward (forward) source in central collisions is possibly greater than or equal to that in peripheral collisions.

d) The event patterns displayed by the scatter plots of charged particles in the three-dimensional velocity space are rough sphericity (or fat ellipsoid along Oz axis) with high density close to $\beta_z = 1$. The event patterns in the three-dimensional momentum space are rough cylinder with some removed particles from the profile. The event patterns in the three-dimensional rapidity space are rough cylinder with a high peak and long tail at the top and bottom respectively. These observations do not depend obviously on the centrality. The effect of anisotropic emission in the transverse plane on the event patterns is not obvious, though v_2 is large in the considered four centrality classes.

Conflict of Interests

The authors declare that there is no conflict of interests regarding the publication of this paper.

Acknowledgments

Comments on the paper from the referee and communications from Edward K. G. Sarkisyan are highly acknowledged. This work was supported by the National Natural Science Foundation of China under Grant No. 11575103, the Shanxi Provincial Natural Science Foundation under Grant No. 201701D121005, and the Fund for Shanxi “1331 Project” Key Subjects Construction.

References

- [1] UA1 Collaboration (G. Arnison *et al.*), Phys. Lett. B **118**, 167 (1982).
- [2] R. Odorico, Phys. Lett. B **118**, 151 (1982).
- [3] T. Mizoguchi, M. Biyajima, N. Suzuki, Int. J. Mod. Phys. A **32**, 1750057 (2017).
- [4] J. Cleymans, H. Oeschler, K. Redlich, S. Wheaton, Phys. Rev. C **73**, 034905 (2006).
- [5] A. Andronic, P. Braun-Munzinger, J. Stachel, Nucl. Phys. A **834**, 237c (2010).
- [6] S. Uddin, J.S. Ahmad, W. Bashir, R.A. Bhat, J. Phys. G **39**, 015012 (2012).

- [7] R.P. Adak, S. Das, S.K. Ghosh, R. Ray, S. Samanta, Phys. Rev. C **96**, 014902 (2017).
- [8] P. Carruthers, M. Doung-van, Phys. Rev. D **8**, 859 (1973).
- [9] BRAHMS Collaboration (I.G. Bearden *et al.*), Phys. Rev. Lett. **88**, 202301 (2002)
- [10] For the BRAHMS Collaboration (M. Murray), J. Phys. G. **30**, S667 (2004).
- [11] BRAHMS Collaboration (I.G. Bearden *et al.*), Phys. Rev. Lett. **94**, 162301 (2005).
- [12] For the BRAHMS Collaboration (M. Murray), J. Phys. G **35**, 044015 (2008).
- [13] C.-Y. Wong, Phys. Rev. C **78**, 054902 (2008).
- [14] E.K.G. Sarkisyan, A.S. Sakharov, AIP Conf. Proc. **828**, 35 (2006).
- [15] E.K.G. Sarkisyan, A.S. Sakharov, Eur. Phys. J. C **70**, 533 (2010).
- [16] E.K.G. Sarkisyan, A.N. Mishra, R. Sahoo, A.S. Sakharov, Phys. Rev. D **93**, 054046 (2016).
- [17] Z.J. Jiang, H.P. Deng, Y. Zhang, H.L. Zhang, Nucl. Phys. Rev. (China) **32**, 398 (2015).
- [18] Z.J. Jiang, H.L. Zhang, Mod. Phys. Lett. A **29**, 1450130 (2014).
- [19] Z.J. Jiang, Y. Zhang, H.L. Zhang, H.P. Deng, Nucl. Phys. A **941**, 188 (2015).
- [20] Y.-H. Chen, G.-X. Zhang, F.-H. Liu, Adv. High Energy Phys. **2015**, 614090 (2016).
- [21] Y.-H. Chen, F.-H. Liu, R.A. Lacey, Adv. High Energy Phys. **2016**, 9876253 (2016).
- [22] Y.-H. Chen, F.-H. Liu, S. Fakhraddin, M.A. Rahim, M.-Y. Duan, J. Phys. G **44**, 025103 (2017).
- [23] Y.-H. Chen, F.-H. Liu, R.A. Lacey, arXiv:1611.10150 [hep-ph] (2016).
- [24] F.-H. Liu, Y.-Q. Gao, T. Tian, B.-C. Li, Eur. Phys. J. A **50**, 94 (2014).
- [25] ALICE Collaboration (B. Abelev *et al.*), Phys. Lett. B **720**, 52 (2013).
- [26] ALICE Collaboration (K. Aamodt *et al.*), Phys. Rev. Lett. **105**, 252302 (2010).
- [27] ALICE Collaboration (J. Adam *et al.*), Phys. Rev. C **93**, 034913 (2016).
- [28] ALICE Collaboration (B. Abelev *et al.*), JHEP **1506**, 190 (2015).
- [29] ALICE Collaboration (J. Adam *et al.*), Phys. Lett. B **754**, 373 (2016).
- [30] ALICE Collaboration (E. Abbas *et al.*), Phys. Lett. B **726**, 610 (2013).
- [31] ALICE Collaboration (K. Aamodt *et al.*), Phys. Rev. Lett. **106**, 032301 (2011).
- [32] L.D. Landau, Izvestiya Akademii Nauk SSSR: Seriya Fizicheskaya **17**, 51 (1953), English translation in *Collected Papers of L.D. Landau* (Pergamon, Oxford), p. 569 (1965).
- [33] S.Z. Belenkiy, L.D. Landau, Soviet Physics Uspekhi **56**, 309 (1955), the shorten English translation in Nuovo Cim. Suppl. **3S10**, 15 (1956).
- [34] ATLAS Collaboration (G. Aad *et al.*), Phys. Lett. B **707**, 330 (2012).
- [35] ATLAS Collaboration (G. Aad *et al.*), Eur. Phys. J. C **74**, 3157 (2014).
- [36] CMS Collaboration (S. Chatrchyan *et al.*), Phys. Rev. C **89**, 044906 (2014).
- [37] On behalf of the CMS Collaboration (S.E. Park), Nucl. Phys. A **967**, 345 (2017).
- [38] NA61/SHINE Collaboration (N. Abgrall *et al.*), Eur. Phys. J. C **74**, 2794 (2014).
- [39] For the NA61/SHINE Collaboration (M. Mackowiak-Pawlowska), Presented at Excited QCD 2017, Sintra, Portugal, 7-13 May 2017, arXiv:1707.04735 [nucl-ex] (2017).
- [40] S. Chatterjee, S. Das, L. Kumar, D. Mishra, B. Mohanty, R. Sahoo, N. Sharma, Adv. High Energy Phys. **2015**, 349013 (2015).
- [41] L.-S. Liu, T.-C. Meng, Phys. Rev. D **27**, 2640 (1983).
- [42] K.-C. Chou, L.-S. Liu, T.-C. Meng, Phys. Rev. D **28**, 1080 (1983).
- [43] Y.B. Ivanov, Phys. Lett. B **721**, 123 (2013).
- [44] Y.B. Ivanov, Phys. Rev. C **87**, 064904 (2013).
- [45] Y.B. Ivanov, D. Blaschke, Phys. Rev. C **92**, 024916 (2015).
- [46] G. Wolschin, Eur. Phys. J. A **5**, 85 (1999).
- [47] G. Wolschin, Prog. Part. Nucl. Phys. **59**, 374 (2007).
- [48] G. Wolschin, EPL **95**, 61001 (2011).
- [49] G. Wolschin, J. Phys. G **40**, 045104 (2013).
- [50] G. Wolschin, Phys. Rev. C **91**, 014905 (2015).
- [51] I. Bautista, C. Pajares, J.G. Milhano, J. Dias de Deus, Phys. Rev. C **86**, 034909 (2012).
- [52] B.-C. Li, Y.-Z. Wang, F.-H. Liu, X.-J. Wen, Y.-E. Dong, Phys. Rev. D **89**, 054014 (2014).
- [53] J. Cleymans, D. Worku, Eur. Phys. J. A **48**, 160 (2012).
- [54] H. Zheng, L.L. Zhu, Adv. High Energy Phys. **2016**, 9632126 (2016).
- [55] E. Schnedermann, J. Sollfrank, U. Heinz, Phys. Rev. C **48**, 2462 (1993).
- [56] Z.B. Tang, Y.C. Xu, L.J. Ruan, G. van Buren, F.Q. Wang, Z.B. Xu, Phys. Rev. C **79**, 051901(R) (2009).
- [57] F.-H. Liu, Y.-Q. Gao, B.-C. Li, Eur. Phys. J. A **50**, 123 (2014).
- [58] R.-F. Si, H.-L. Li, F.-H. Liu, arXiv:1710.09645 [nucl-th] (2017).
- [59] P. Bozek, Eur. Phys. J. C **71**, 1530 (2011).
- [60] A.N. Mishra, R. Sahoo, E.K.G. Sarkisyan, A.S. Sakharov, Eur. Phys. J. C **74**, 3147 (2014).
- [61] E.K.G. Sarkisyan, A.N. Mishra, R. Sahoo, A.S. Sakharov, Phys. Rev. D **94**, 011501(R) (2016).
- [62] C. Patrignani *et al.* (Particle Data Group), Chin. Phys. C **40**, 100001 (2016).